

## Supplementary Information for

Three-dimensional optical trapping and orientation of microparticles for coherent X-ray diffraction imaging

Yuan Gao<sup>1,\*</sup>, Ross Harder<sup>1</sup>, Stephen H. Southworth<sup>1</sup>, Jeffrey R. Guest<sup>1</sup>, Xiaojing Huang<sup>2</sup>, Zijie Yan<sup>3,4</sup>, Leonidas E. Ocola<sup>1</sup>, Yuval Yifat<sup>3</sup>, Nishant Sule<sup>3</sup>, Phay J. Ho<sup>1</sup>, Matthew Pelton<sup>5</sup>, Norbert F. Scherer<sup>1,3</sup>, and Linda Young<sup>1,6,\*</sup>

<sup>1</sup> Argonne National Laboratory, Lemont, IL 60439

<sup>2</sup> Brookhaven National Laboratory, Upton, NY 11973

<sup>3</sup> Department of Chemistry and James Franck Institute, University of Chicago, Chicago, IL 60637

<sup>4</sup> Department of Chemical and Biomolecular Engineering, Clarkson University, Potsdam, NY 13699

<sup>5</sup> Department of Physics, University of Maryland, Baltimore County, MD 21250

<sup>6</sup> Department of Physics and James Franck Institute, University of Chicago, Chicago, IL 60637

\* Email: [juangao@bnl.gov](mailto:juangao@bnl.gov); [young@anl.gov](mailto:young@anl.gov)

Corresponding author: Yuan Gao, Linda Young  
Email: [juangao@bnl.gov](mailto:juangao@bnl.gov), [young@anl.gov](mailto:young@anl.gov)

### **This PDF file includes:**

Supplementary text  
Figures S1 to S5  
Captions for videos S1 to S5  
References for SI reference citations

### **Other supplementary materials for this manuscript include the following:**

Videos S1 to S5

## Supplementary Information Text

**Multi-focus standing-wave optical trap for sample manipulation.** To minimize the energy absorbed by the sample, the wavelength of the trapping laser is chosen to be 1064 nm, which is in the near-infrared window for biologic in-vivo imaging. The corresponding photon energy, 1.16 eV, is smaller than the bandgap of most common semiconducting minerals (1).

We utilized the holographic beam shaping technique and an in-situ micro-mirror to form the multi-focus standing wave trap. As shown in Figure S1, by adding a binary zone plate phase to the laser beam, two series of focal planes (i.e. positive and negative orders) were generated after being focused by a microscope objective. The focal planes located symmetrically on both sides of the original focal plane, and the distance between them could be adjusted by re-programming the phase pattern displayed on the SLM. By placing a mirror at the focal plane of the unmodified laser beam, all the positive order foci are reflected by the mirror and overlap with the negative order foci, forming a series of standing wave patterns in the longitudinal direction. The efficiency of each order was dictated by the phase pattern. As for the binary zone plate, the first order standing wave focus contains  $\sim 80\%$  power of the full beam(2).

Multiple 1st order standing wave foci are necessary to align and orient anisotropic particles. These can be generated either by adding a binary grating phase to the zone plate or by mixing multiple zone plates via random mask encoding (RME) method(3) (Figure S1e). The latter method (i.e. mixing multiple zone plates via RME) has the advantage that the longitudinal position of every 1st order standing wave focus can be adjusted individually, while the former method (i.e. combining binary grating phase and zone plate phase) can generate multiple 1st order standing wave foci only in the same lateral plane.

The rotations in three dimensions were controlled in different ways:

(a) Rotation of the trapped cylindrically-shaped particle in the horizontal plane (i.e. rotation around the  $y'$ -axis in Figure 1c) was controlled by moving the foci in the horizontal plane. This was done by rotating the whole phase pattern displayed on the SLM. Limited by the number of pixels on the SLM screen (512 pixels x 512 pixels) and the  $15\ \mu\text{m} \times 15\ \mu\text{m}$  pixel size, rotating the phase pattern could only achieve  $\sim 2$  milli-radian resolution. To overcome this limitation, after finding the Bragg peak, the rocking curve scan was performed by physically rotating the whole SLM around the center of the SLM screen (as shown in Figure S1f).

(b) To rotate the particle around the  $z'$ -axis (see Figure 1c), the vertical positions of the two foci must be tuned separately. This can be done only if the phase pattern is generated by RME. While providing this unique function, RME method adds artificial noise to the phase pattern, resulting in a slightly lower trapping stiffness.

(c) To control the rotation around the long axis of the cylindrically-shaped particle (i.e.  $x'$ -axis in Figure 1c), at least three noncollinear foci are required. However, limited by the sub-micron diameter of the particle, we were not able to apply the third focus. This angle was aligned by the interaction between the laser and the prism-shaped particle (as shown in Figure 3d).

**Laser and optical trapping setup.** To combine the laser beam, the X-ray beam, and the in-situ nano-mirror, we fabricated a microfluidic cell by etching Si wafer. A schematic of the optical trapping apparatus is shown in Figure S2. The optical trap was roughly aligned by positioning the sample cell to the X-ray beam. The X-ray beam was focused into an approximately  $1.0\ \mu\text{m}$  (H) x

0.8  $\mu\text{m}$  (V) spot by Kirkpatrick-Baez (KB) mirrors and propagated through the microfluidic sample cell (see Figure S2a). To optimize the spatial overlap of the laser focus and the X-ray focus, we trapped a  $\sim 1$   $\mu\text{m}$  X-ray phosphor particle and brought the X-ray beam to the trapped particle by adjusting the position of the KB mirrors. After achieving the desired spatial overlap, all the sample manipulations, including rotations and translations, were done by altering the shape of the optical trap (i.e. modifying the phase pattern displayed on the SLM).

**Measurement of X-ray diffraction.** Owing to the limited vertical aperture, the incident and diffracted X-ray beams were in the  $x - z$  plane, where  $z$  was the downstream direction and  $x$  was the outboard direction. In this experiment, we observed the [002] Bragg diffraction from the ZnO wurtzite lattice. The [002] lattice planes are perpendicular to the long axis of the ZnO rod. By moving the sample cell horizontally, we could select and trap the desired particle, which was initially sitting on the bottom surface of the fluidic channel. However, trapping near the bottom surface was not stable, and other particles could accidentally jump into the trap. To improve the trapping stability and avoid the influence of other particles, the selected particle was trapped and translated to the top of the cell and the Au mirrored surface and robustly trapped by the standing wave, which was located approximately 10 microns below the gold mirror.

**Angular variance and trapping stiffness.** The angular trapping stiffness is estimated using the equipartition theorem

$$\frac{1}{2}k_B T = \frac{1}{2}\kappa_{rot}\langle(\Delta\theta)^2\rangle$$

where  $\langle(\Delta\theta)^2\rangle$  is the variance of the angular position. Therefore, the angular variance is

$$\langle(\Delta\theta)^2\rangle = \frac{k_B T}{\kappa_{rot}} \quad (\text{S1})$$

The angular trapping stiffness  $\kappa_{rot}$  can be converted to the translational stiffness  $\kappa$  using the definition of the trapping stiffness

$$\text{Torque} = -\kappa_{rot} \cdot \Delta\theta = 2 \cdot (-\kappa \cdot \Delta z') \cdot \frac{1}{2}D$$

where  $\Delta\theta$  is the angular displacement,  $\Delta z'$  is the translational displacement of the ends of the rod in the  $z'$  direction,  $D$  is the length of the rod (the rotation center is set at the middle point of the rod and the two laser foci are at the ends of the rod). Since  $\Delta z' = \Delta\theta \cdot \frac{1}{2}D$ , we have

$$\kappa_{rot} = \frac{1}{2}\kappa D^2$$

Substitute into Eq. S1, we have

$$\langle(\Delta\theta)^2\rangle = \frac{2k_B T}{\kappa D^2} \quad (\text{S2})$$

**Spatial resolution of phase retrieval.** The resolution of the 3D reconstruction was characterized via the phase retrieval transfer function (PRTF), which measures the reproducibility of the retrieved phases. The resolution is given as when the PRTF drops below a certain value (see Figure S4a). The PRTF is defined as

$$\text{PRTF}(\mathbf{Q}) = \frac{|\mathcal{F}\{\Phi(\mathbf{Q})\}|}{\sqrt{I(\mathbf{Q})}}$$

where  $I(\mathbf{Q})$  is the measured diffraction intensity, and  $\Phi(\mathbf{Q})$  is the best reconstruction obtained at the end of the guided algorithm approach. The numerator is the amplitude of the Fourier transform of  $\Phi(\mathbf{Q})$ . A conservative estimate of the resolution is when the PRTF drops below 0.5(4). Therefore, the resolution was estimated to be 60 nm. The spatial resolution was verified via a line cut through the boundary of the crystalline grain. As shown in Figure S4b, the 10% to

90% edge response gives a resolution of 50 nm. The real space grid spacing of the reconstruction is 8 nm, which accounts for the discrepancy.

**Estimation of the required laser foci spacing for performing Bragg CXDI on optically trapped objects.** To trap an object that is stable enough for the Bragg CXDI measurement, the angular fluctuation of the trapped object must be less than the speckle size that needs to be resolved. Therefore, from Eq. S2, we have

$$\sqrt{\frac{2k_B T}{\kappa D^2}} < \frac{\lambda}{d}$$

where  $D$  is the distance between the two Gaussian foci,  $d$  is the size of the feature that we want to resolve,  $\kappa$  is the trapping stiffness,  $\lambda$  is the wavelength of the coherent X-ray beam,  $k_B$  is the Boltzmann constant, and  $T$  is the temperature. The requirement can be written as

$$\frac{D}{d} > \sqrt{\frac{2k_B T}{\kappa \lambda^2}} \quad (\text{S3})$$

According to Eq. S3, the ability to hold an object with angular stability necessary for the Bragg CXDI is tied to the ratio of the laser foci spacing  $D$  and the feature size  $d$ . Considering the Bragg CXDI measurement described in the main text,  $d$  was the largest dimension of the crystalline grain ( $\sim 700$  nm), and the laser foci spacing  $D$  was 18  $\mu\text{m}$ . If we perform Bragg ptychography instead of the traditional Bragg CXDI,  $d$  is dictated by the size of the coherent X-ray beam focus, which can be 50 nm(5) or smaller. Assuming that we perform Bragg ptychography with a coherent X-ray beam focused to 100 nm, the required spacing  $D$  between the laser foci is only 2.5  $\mu\text{m}$ .

**Thermal calculation for the trapped particle.** We estimated the laser-induced temperature rise of the trapped ZnO cylindrically-shaped particle. To simplify the calculation, the particle was assumed to be a uniform rod with a hexagonal cross-section. The particle was held by two laser foci at the ends of the rod, respectively. The laser-illuminated part of the particle was assumed to have a uniform temperature distribution. The water surrounding the particle was considered as a heat sink at room temperature (298 K).

As shown in Figure S5,  $L$  is the length of the ZnO rod,  $r$  is the edge of the hexagonal cross section. Both ends of the rod are illuminated by laser beams with  $1/e^2$  diameter  $w$ . The part under the laser illumination, i.e. region 1, is considered separately from the rest of the particle (region 2).

For region 1, according to the law of heat conduction and convection(6), the heat flows into and out of the region 1 within time interval  $\Delta t$  are

$$Q_{in}^{(1)} = P_{laser} \cdot \eta \cdot \Delta t$$

$$Q_{out\_conv}^{(1)} = h\Delta T A_1 \Delta t = h \cdot [T_1(t) - T_{rm}] \cdot [6rw + \frac{3\sqrt{3}}{2} r^2] \cdot \Delta t$$

$$Q_{out\_cond}^{(1)} = -k\nabla T A_{int} \Delta t = -k \frac{\partial T_2(x, t)}{\partial x} \Big|_{x=\pm(\frac{1}{2}L-w)} \cdot \frac{3\sqrt{3}}{2} r^2 \cdot \Delta t$$

where  $P_{laser}$  is the laser power,  $\eta$  is the absorptance,  $k$  is the thermal conductivity of ZnO,  $h$  is the heat transfer coefficient between ZnO particle and water,  $T_1(t)$  is the temperature of region 1,  $T_2(x, t)$  is the temperature distribution in region 2,  $T_{rm}$  is the room temperature,  $A_1$  is the surface

area of region 1, and  $A_{int}$  is the intersection area between region 1 and 2. Therefore, the heat gain of region 1 and the corresponding temperature change  $\Delta T_1$  can be written as

$$Q_{in}^{(1)} - Q_{out\_conv}^{(1)} - Q_{out\_cond}^{(1)} = c\rho V_1 \Delta T_1 \quad (S4)$$

where  $c$  and  $\rho$  are the specific heat and density of ZnO, and  $V_1$  is the volume of region 1.

For region 2, we consider the heat transfer in a section with length  $\Delta x$  at position  $x$ . Similarly, the heat flows into and out of the section are

$$Q_{in\_cond}^{(2)} = -k\nabla T A_{int} \Delta t = -k \frac{\partial T_2(x, t)}{\partial x} \cdot \frac{3\sqrt{3}}{2} r^2 \cdot \Delta t$$

$$Q_{out\_cond}^{(2)} = -k \frac{\partial T_2(x + \Delta x, t)}{\partial x} \cdot \frac{3\sqrt{3}}{2} r^2 \cdot \Delta t$$

$$Q_{out\_conv}^{(2)} = h \cdot [T_2(x, t) - T_{rm}] \cdot 6r\Delta x \cdot \Delta t$$

where  $6r\Delta x$  is the surface area of the section. Then we have

$$Q_{in\_cond}^{(2)} - Q_{out\_cond}^{(2)} - Q_{out\_conv}^{(2)} = c\rho V_{sec} \Delta T_2 \quad (S5)$$

The Eq. S4 and S5 can be written as

$$\eta P_{laser} + k \frac{\partial T_2(x, t)}{\partial x} \Big|_{x=\pm(\frac{1}{2}L-w)} \cdot \frac{3\sqrt{3}}{2} r^2 - h \cdot [T_1 - T_{rm}] \cdot [6rw + \frac{3\sqrt{3}}{2} r^2] = c\rho \frac{3\sqrt{3}}{2} r^2 w \frac{\partial T_1}{\partial t} \quad (S6)$$

$$-k \frac{\partial T_2(x, t)}{\partial x} \cdot \frac{3\sqrt{3}}{2} r^2 + k \frac{\partial T_2(x+\Delta x, t)}{\partial x} \cdot \frac{3\sqrt{3}}{2} r^2 - h \cdot [T_2(x, t) - T_{rm}] \cdot 6r\Delta x = c\rho \frac{3\sqrt{3}}{2} r^2 \Delta x \frac{\partial T_2}{\partial t} \quad (S7)$$

In the heat equilibrium status, the temperature distribution in the rod is static, i.e.  $\partial T / \partial t = 0$ . Therefore, Eq. S6 and S7 become

$$\eta P_{laser} = h \cdot [T_1 - T_{rm}] \cdot \left[ 6rw + \frac{3\sqrt{3}}{2} r^2 \right] - k \frac{\partial T_2(x, t)}{\partial x} \Big|_{x=\pm(\frac{1}{2}L-w)} \cdot \frac{3\sqrt{3}}{2} r^2$$

$$\frac{\partial^2 T_2(x, t)}{\partial x^2} = \frac{4}{\sqrt{3}} \frac{h}{kr} \cdot [T_2(x, t) - T_{rm}]$$

Two boundary conditions are required to solve these equations. At the intersection between region 1 and 2, the temperature of region 2 should equal the temperature of region 1

$$T_2 \Big|_{x=\pm(\frac{1}{2}L-w)} = T_1$$

Meanwhile, due to the symmetry of the system, the temperature distribution  $T_2$  should be symmetric with respect to the point  $x = 0$ , i.e. the center of the ZnO particle. Using these two boundary conditions, we get

$$T_1 = T_{rm} + \zeta \cdot [e^{-(\frac{1}{2}L-w)\sqrt{\delta}} + e^{(\frac{1}{2}L-w)\sqrt{\delta}}]$$

$$T_2 = T_{rm} + \zeta \cdot [e^{-\sqrt{\delta} \cdot x} + e^{\sqrt{\delta} \cdot x}]$$

where

$$\delta = \frac{4}{\sqrt{3}} \cdot \frac{h}{kr}$$

$$\zeta = \frac{\eta P_{laser}}{\epsilon_+ h \cdot \left[ 6rw + \frac{3\sqrt{3}}{2} r^2 \right] - \epsilon_- k \sqrt{\delta} \cdot \frac{3\sqrt{3}}{2} r^2}$$

$$\epsilon_{\pm} = e^{-\left(\frac{1}{2}L-w\right)\sqrt{\delta}} \pm e^{\left(\frac{1}{2}L-w\right)\sqrt{\delta}}$$

In our experiment, the maximum laser power measured at the incident aperture of the objective is 400 mW. Due to the ~50% transmission of the microscope objective at 1064 nm and the dual-focus trapping,  $P_{laser}$  is about 100 mW. Considering an 18  $\mu\text{m}$  long ZnO rod with 0.5  $\mu\text{m}$  diameter, we have  $r = 250$  nm and  $\eta = 2.5 \times 10^{-4}$  (7). Information about the thermal conductivity of individual ZnO nanowires, as well as the heat transfer coefficient between an individual ZnO nanoparticle and the surrounding water, is lacking. A conservative estimate is  $k = 10$  W/m/K (8, 9) and  $h = 1.0 \times 10^6$  W/m<sup>2</sup>/K (10, 11). The resultant temperature rise in the trapped ZnO particle is ~6 °C at the ends and ~0.01 °C at the center.

**Significant particle-to-particle variation in the dissolution of ZnO particles.** We observed radiation-induced dissolution of certain ZnO particles during the diffraction measurements (as shown in Supplemental Video 3). Both the length and the diameter of the trapped particle reduced significantly in about 10 minutes. As a comparison, similar particles could behave completely differently under the same conditions (see Supplemental Video 4 and 5). In latter cases, no significant change in diffraction intensity was observed after about 30 minutes of X-ray illumination, suggesting that the lattice structure of the trapped ZnO particle did not change.

To understand the cause of this phenomenon, we compared the sample lifetime under various situations, such as different X-ray photon energies (i.e. above or below the Zn K-edge), different laser powers and polarizations, as well as ZnO samples with various surface treatments. This radiation damage behavior, which seemed to happen only when the particle was illuminated by X-rays, was not related to the X-ray photon energy or the laser power. In the future, we will test other materials to investigate the mechanism of this behavior.

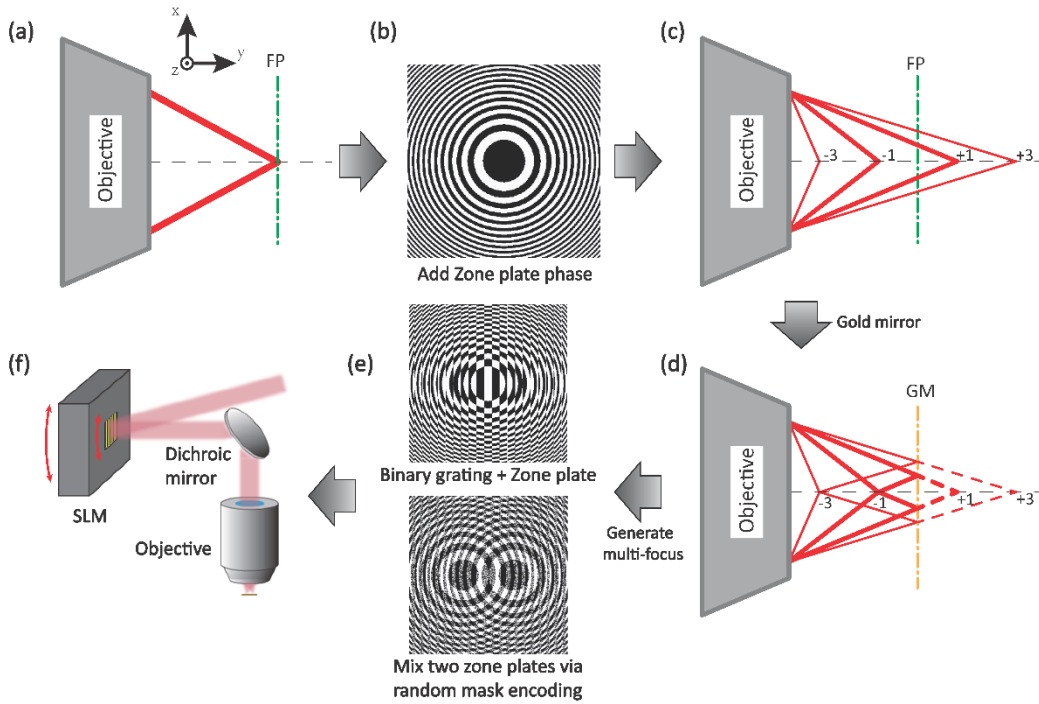


**Figure S1. Two standing wave foci generated by holographic beam shaping.** (a) Original focal plane (FP) of the microscope objective with a collimated laser beam. (b) Binary zone plate phase displayed on the SLM. (c) The modified laser beam is focused by the objective and generates multiple foci along the beam axis. The diverging light after each focus is not shown. The intensity of the diverging light decreases with the square of the distance from the focus. Because of the high divergence ( $NA = 1.2$ ), the interference between the diverging light and the downstream focus is negligible. (d) A gold mirror (GM) is placed at the focal plane of the unmodified optical beam and reflects the laser beam. The reflected positive foci overlap with the negative foci and generate standing waves. The drawings in (a), (c) and (d) are not to scale. The distance between the microscope objective and the focal plane is  $\sim 250 \mu\text{m}$ . The  $\pm 1$  order foci are  $\sim 10 \mu\text{m}$  away from the original focal plane. (e) Multi 1st order standing wave foci can be generated by either adding a binary grating phase to the zone plate (top) or mixing two zone plates via random mask encoding (bottom). (f) Rotation of the multi 1st order foci is conducted by either rotating the phase pattern displayed on the SLM (low resolution) or physically rotating the SLM (high resolution).

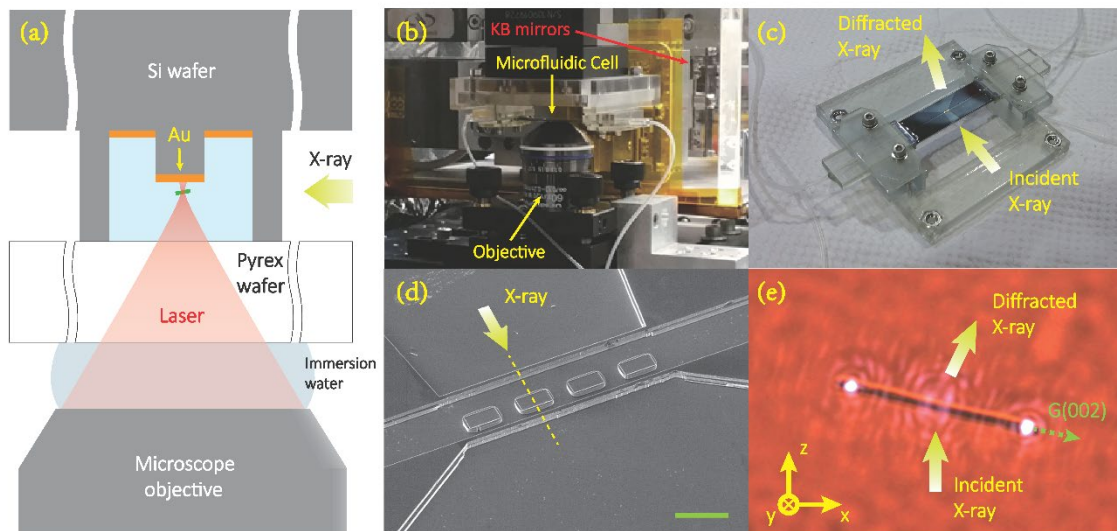


**Figure S2. Schematic of the sample cell setup.** (a) Cross section of the setup along the dashed line in (d). (b) A photo of the setup taken from the downstream side. (c) A microfluidic sample cell mounted on the 3D-printed holder. During the experiment, the transparent side of the cell is facing down. (d) SEM image of the microfluidic channel. The scale bar in (d) is 500  $\mu\text{m}$ . (e) The bottom view of a trapped  $\sim 15$   $\mu\text{m}$  long ZnO rod. This bright-field image was taken during the experiment by the microscope objective in the optical trapping apparatus. The rod was trapped by a dual-focus standing wave trap (two bright spots). The coordinates are defined as  $x$  – outboard,  $y$  – upward, and  $z$  – downstream of the X-ray beam. The laser was propagating upward.

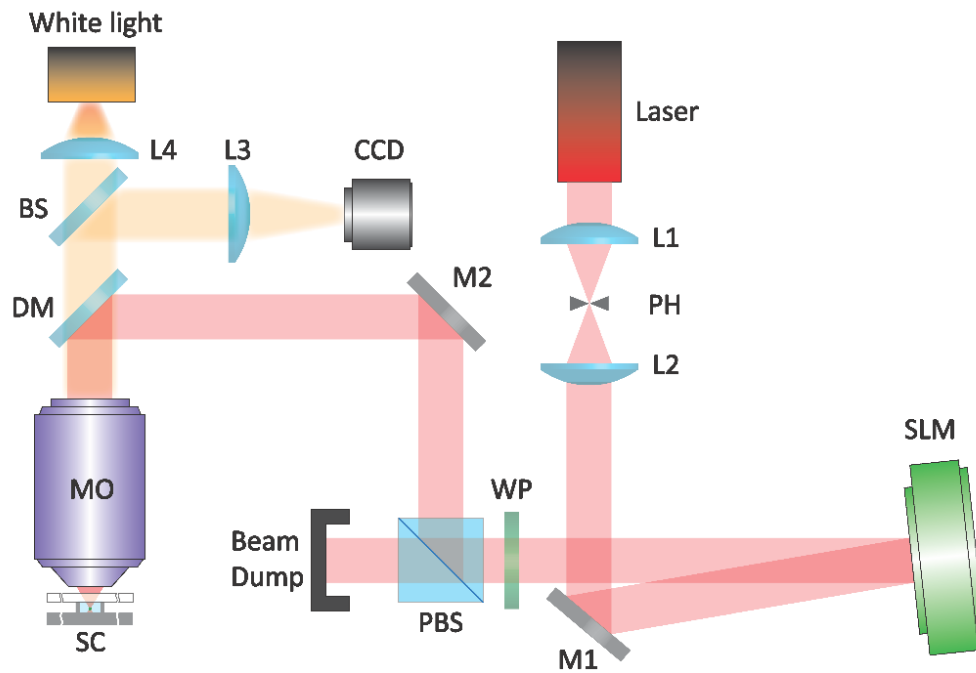


**Figure S3. Schematic of the laser and optical trapping setup.** The IR laser path and white light path are indicated (L: lens; PH: pinhole; M: mirror; WP: half-wave plate; PBS: polarizing beam splitter; DM: dichroic mirror; MO: microscope objective; SC: sample cell; BS: 50-50 beam splitter for white light). The 4-f optical system between the SLM and the microscope objective is not shown in this diagram.

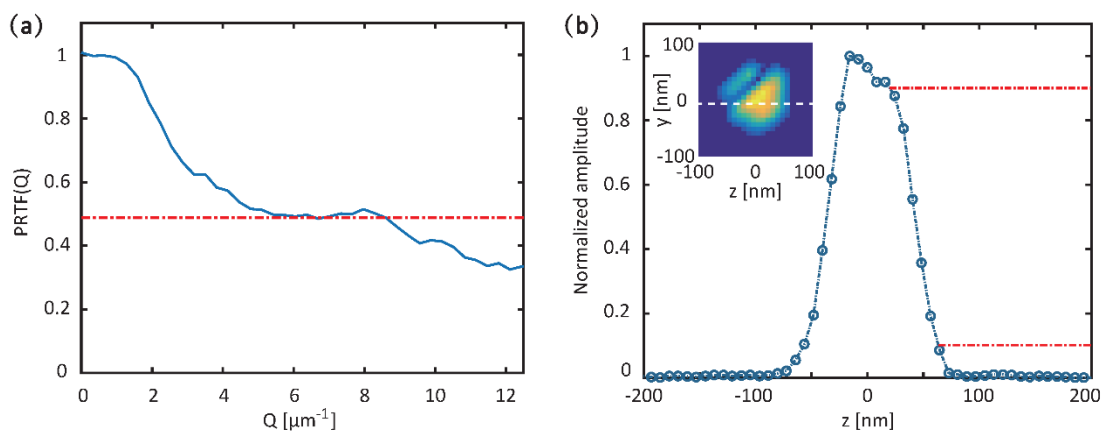


**Figure S4. Resolution of the CXDI reconstruction determined from the Phase Retrieval Transfer Function.** (a) The phase retrieval transfer function of a reconstruction. Defining a cutoff of 0.5 predicts a spatial resolution of 60 nm. (b) A line cut through the boundary of the crystalline grain. The 10% to 90% edge response gives a resolution of 50 nm.

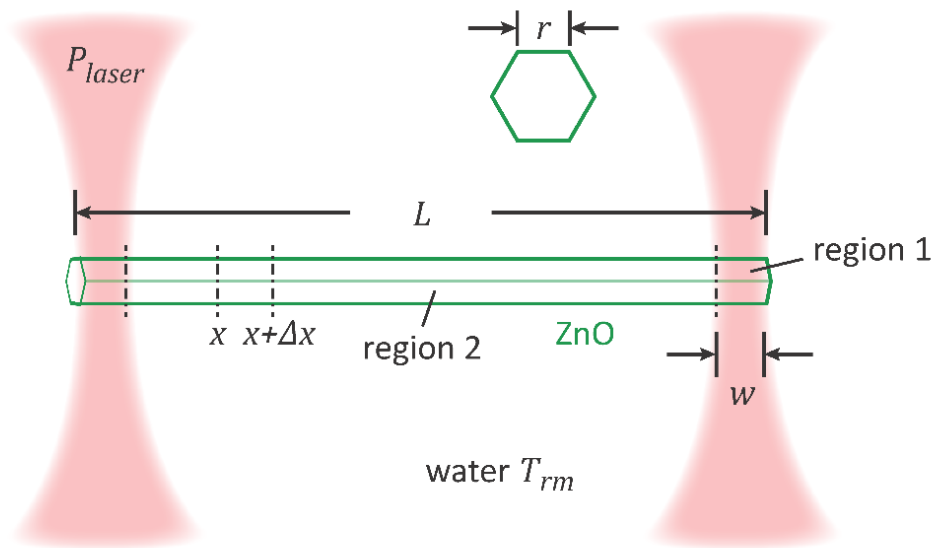


**Figure S5. Schematic of the thermal calculation for the trapped particle.** A ZnO cylindrically-shaped particle with length  $L$  and cross section edge  $r$  is trapped by dual-focus optical trap. Each focus has a power  $P_{laser}$  with  $1/e^2$  diameter  $w$ . The water surrounding the particle is at room temperature  $T_{rm}$ .

**Video S1. Precise control of the tilting angle of a trapped ZnO microparticle.** The Bragg diffraction peak, which was initially partially blocked, can be viewed in full by adjusting the position of each end of the particle along the laser propagation direction. The particle was trapped by the multi-focus standing wave trap that generated by random mask encoding method.

**Video S2. Rocking curve scan of an optically trapped ZnO rod.** The particle was trapped by the multi-focus standing wave optical trap. The orientation of the particle was precisely rotated through a Bragg peak by physically rotating the whole SLM around the center of the SLM screen.

**Video S3. Radiation-induced dissolution of an optically trapped ZnO particle during the diffraction measurement. (15x fast-forward playback)** An approximately 10  $\mu\text{m}$  long ZnO particle was trapped by two standing wave foci (bright spots near the ends of the rod). This video was taken with the same microscope objective that focused the laser. The incident X-ray beam propagated from bottom to top in the field of view and was focused at the middle point between the two laser foci. Both the diameter and the length of the trapped particle reduced significantly over the duration of this video due to the radiation-induced dissolution. The trapping configuration was adjusted dynamically to compensate this morphology change and maintain a stable trap of the particle.

**Video S4. An optically trapped ZnO particle during the rocking curve scan. (15x fast-forward playback)** This particle was trapped under the same condition as the particle in Supplemental video 3. Bragg CXDI measurement shown in the manuscript was performed while taking this video. For example, at approximately 00:12 of this video, a 1 degree rotation of the particle can be observed, indicating the rocking curve scan for the Bragg CXDI measurement. Global deposition over the surface of the trapped crystal was observed. The diameter of the trapped particle increased by approximately a factor of 2 compared to the original shape (shown in Figure 4 inset).

**Video S5. X-ray induced deposition on the surface of an optically trapped ZnO particle. (15x fast-forward playback)** A  $\sim 20$   $\mu\text{m}$  long particle was trapped under the same condition as Supplemental video 3 and 4. The X-ray beam was focused on the middle part of the particle. Obvious surface deposition, which started from the X-ray illuminated region, was observed over the  $\sim 20$  min duration. The deposited material was semi-transparent under the optical microscope. Such surface deposition did not affect the intensity of the diffraction peak, suggesting the deposited material was likely composed of low Z elements, such as hydrocarbon.

## References

1. Xu Y, Schoonen MAA (2000) The absolute energy positions of conduction and valence bands of selected semiconducting minerals. *American Mineralogist* 85(3–4):543–556.
2. Diffraction Efficiency of Gratings (2007). *Holographic Imaging* (Wiley-Blackwell), pp 57–63.
3. Montes-Usategui M, Pleguezuelos E, Andilla J, Martin-Badosa E (2006) Fast generation of holographic optical tweezers by random mask encoding of Fourier components. *Optics Express* 14(6):2101–2107.

4. Clark JN, et al. (2015) Three-dimensional imaging of dislocation propagation during crystal growth and dissolution. *Nature Materials* 14(8):780–784.
5. Hill MO, et al. (2018) Measuring Three-Dimensional Strain and Structural Defects in a Single InGaAs Nanowire Using Coherent X-ray Multiangle Bragg Projection Ptychography. *Nano Lett* 18(2):811–819.
6. Çengel YA (2004) *Heat transfer : a practical approach* (McGraw-Hill, New York).
7. Polyanskiy MN *Refractive index database* Available at: <https://refractiveindex.info>.
8. Wu X, et al. (2016) Thermal conductivity of wurtzite zinc-oxide from first-principles lattice dynamics – a comparative study with gallium nitride. *Scientific Reports* 6:22504.
9. Xu Y, Goto M, Kato R, Tanaka Y, Kagawa Y (2012) Thermal conductivity of ZnO thin film produced by reactive sputtering. *Journal of Applied Physics* 111(8):084320.
10. Merabia S, Shenogin S, Joly L, Keblinski P, Barrat J-L (2009) Heat transfer from nanoparticles: A corresponding state analysis. *Proc Natl Acad Sci USA* 106(36):15113.
11. Lienhard IV JH, Lienhard V JH (2018) *A Heat Transfer Textbook* (Phlogiston Press, Cambridge, MA). 4th Ed. Available at: <http://ahtt.mit.edu>.